



Research paper

Tailoring structured WGS catalysts: Impact of multilayered concept on the water surface interactions

M. González-Castaño*, E. Le Saché¹, S. Ivanova, F. Romero-Sarria, M.A. Centeno, J.A. Odriozola*Departamento de Química Inorgánica e Instituto de Ciencia de Materiales de Sevilla, Centro mixto Universidad de Sevilla-CSIC, Avda. Américo Vespucio 49, 41092 Sevilla, Spain*

ARTICLE INFO

Keywords:

Structured WGS catalysts
Metallic monoliths
Ceria
Oxygen vacancy
Water splitting
Water absorption
Water desorption
H₂O-TPD
FT-IR

ABSTRACT

A novel multilayer approach for designing structured WGS catalyst is employed in this study as a response to the lack of new strategies in the literature. The approach proposes the use of two successive layers with different functionalities on metallic micromonolith substrate. The WGS catalyst behavior is modulated by the nature of the inner layer which determines the active species surface population by acting on the water activation step. The catalytic promotion attained by introducing inner ceria containing solids with increasing number of oxygen defects is intensely analyzed through FT-IR and H₂O-TPD. Several evidences about the participation of the oxygen vacancies, as key sites, for water absorption processes are established. Besides, remarkable relationships between the water absorption strengths and the water splitting processes within their influence on the catalyst performance are also discussed.

1. Introduction

Among the new green energies, H₂ appears as a promising vector. However, its success relies on the removal of CO coproduced with H₂ in the reformat process in order to avoid the poisoning of the Pt-based anode of the Polymeric Exchange Membranes Fuel Cells (PEMFC). The water gas shift (WGS, CO + H₂O → CO₂ + H₂) reaction allows CO removal at the same time that increases the H₂ concentration. The reaction is also moderately exothermic and equilibrium limited, therefore, the control of the temperature is a crucial task [1]. Moreover, WGS reaction is characterized by high contact times and as a result, high reactor volume are necessary to achieve good catalytic performances [2].

The industrially established WGS process is not well suited for small-scale applications, such as residential fuel cells or on-board hydrogen generators, for which reduced volume and weight catalytic beds are required. In fact, on-board portable applications intrinsically demand long lasting and highly active catalytic systems which should also support fast start-up and shutdown conditions. Attending to the mobile device power requirements, the drawbacks presented by the traditional WGS catalysts, e.g. slow response to transient operation of flow rate and temperature, could be overpassed applying noble metal (NM) based catalysts [1,3]. Within the reported NM catalysts, those based on Pt formulations appear as the best solutions especially when coupled with

ceria containing support [4–7]. The use of ceria presumably intensifies the rate of WGS CO conversion by increasing the water activation rate due to its advantageous electronic properties which are, in turn, intimately associated to its structural defects, i.e. oxygen vacancies (Ov) [8,9]. So, the attention received by the oxygen defects lies on its capacity for dissociating water species and on the concomitant enhancement of the WGS catalyst' reaction rates [10,11]. A possible way to control and increase the number of oxygen defect sites within ceria matrix is its doping with trivalent metal in proportion where the formation of solid solution is observed [12–18].

Nevertheless, not only the catalyst but also the reactor design is of crucial importance for the WGS process on-board applications [2]. An optimal structured reactor design should solve practical problems arising from WGS reaction particularities. The desired performance criteria for catalysts bed are low pressure drop, high catalyst loading per reactor volume, high external fluid to catalyst mass and heat transfer rates and high internal mass transfer rate within the catalyst [19–22]. In this context, parallel channel metallic micromonoliths appear as an attractive alternative from their inherent high thermal conductivities which assure enhanced heat transfer managements and allow shorter contact times, reduced transport limitations and higher catalyst surface-to-volume ratios. As a result, metallic micromonoliths should lead to compact catalytic beds and, then, to increased overall process efficiencies.

* Corresponding author. Present address: EMPA, Swiss Federal Laboratories for Material Science and Technology, Ueberlandstrasse 129, 8600 Dübendorf, Switzerland.

E-mail address: Mirian.Gonzalez-Castano@empa.ch (M. González-Castaño).

¹ Present address: Department of Chemical and Process Engineering, University of Surrey, GU2 7XH Guildford, United Kingdom.

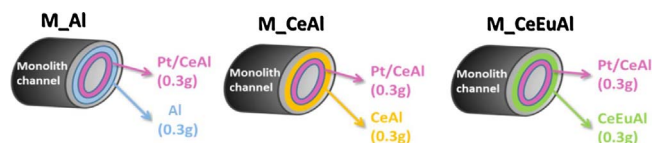


Fig. 1. Schematic representation of the prepared structured catalysts.

In a previous work [20], the oxygen vacancies and metallic micromonoliths benefits were merged on the development of a novel structured catalyst composed by two consecutive layers with different tasks: an inner layer of material able to absorb water and release activated water species in continuous manner and an outer catalyst layer where the WGS reaction should occur. The greater WGS overall reaction rate in presence of the inner layer was related to superior apparent H_2O partial kinetic orders and consequently, to higher H/OH species population in the vicinity of the Pt active sites.

From the introduction of the multilayered concept, this work provides an intense analysis of the role of the buffer layer as a function of its water splitting capacity. The studied structured catalytic systems are schematically presented in Fig. 1. For that purpose, Pt(2%)/ CeO_2/Al_2O_3 was maintained as catalyst for the all structured catalyst outer layers meanwhile the nature of the inner layer, named buffer layer, was varied. Three buffer materials differing on their water splitting capacity were chosen:

- $\gamma-Al_2O_3$ chosen for its chemical similarity to oxidized stainless steel monolith surface and more importantly because of low available number of oxygen defect sites for water activation. In fact, this material is generally considered as inactive support for WGS reaction [32,33];
- CeO_2/Al_2O_3 chosen as material with similar textural properties to that of $\gamma-Al_2O_3$ but with increased number of oxygen defect sites due to the presence of CeO_2 surface layer;
- $Ce_{0.9}Eu_{0.1}O_2/Al_2O_3$ chosen for its expected intensification of the oxygen vacancies concentration due to Eu^{3+} to Ce^{4+} substitution and solid solution formation accompanied by oxygen defects formation via charge compensation mechanism [18]. In addition, Eu_2O_3 do not possess by itself any intrinsic activity for the WGS reaction.

Hence, as an initial hypothesis, one could expect that the WGS activity sequence should correlate directly to buffer's ability to activate water, presumably in the following descending activity order $Ce_{0.9}Eu_{0.1}O_2/Al_2O_3 > CeO_2/Al_2O_3 > \gamma-Al_2O_3$. The use of Pt(2%)/ CeO_2/Al_2O_3 catalyst prepared in one unique batch with equivalent properties (chemical composition, metal dispersion etc.) consent ascribing the observed changes uniquely to the buffer layer role.

Therefore, this study offers a tuning procedure for enhanced WGS structured catalysts at the same time as it delivers a comprehensive analysis of the water ceria surface interactions which, depending on defect surface population, tailor the WGS catalytic behaviors. In fact, the application of the multilayer approach pretends to prove the design suitability and to highlight it as a potential strategy for achieving advanced structured WGS catalysts.

2. Materials and methods

2.1. Preparation of metallic micromonolith substrates

The micromonoliths were prepared by rolling up flat and corrugated ferritic stainless steel a foil (Fecralloy) around a spindle. The resulting structures are cylinders of 1.6 cm diameter, 3 cm height and 540 cm^2 geometric surface area with cell density of 2067 cpsi. The micromonoliths were thermally pretreated during 22 h at 900°C in order to generate $\alpha-Al_2O_3$ oxidized surface layer for better catalyst adhesion

during the deposition assured by roughness increase for physical anchorage and chemical compatibility [23,24].

2.2. Catalyst and buffer synthesis

The CeO_2/Al_2O_3 and the $Ce_{0.9}Eu_{0.1}O_2/Al_2O_3$ buffer materials were prepared by wet impregnation of their respective nitrates over a commercial $\gamma-Al_2O_3$ (Sasol). The $CeO_2(Ce_{0.9}Eu_{0.1}O_2):Al_2O_3$ ratio was fixed to 20:80 (wt.%). For each solid, the adequate precursor amounts were dissolved into ethanol solution and added over the commercial $\gamma-Al_2O_3$ under stirring for ensuring the solution homogeneity. Some ethanol was added until the $\gamma-Al_2O_3$ powder was completely covered. The resulting suspension was concentrated (almost dry) by evaporating the ethanol under reduced pressure. The obtained dry solid was treated with diluted NH_3 (10 M) solution during 30 min, filtered and rinsed with deionized water. The resulting powder is dry during 12 h at 120°C , grinded and calcined at 450°C for 4 h at $10^\circ\text{C}/\text{min}$ heating rate. The as prepared buffers are denominated Al, CeAl and CeEuAl for Al_2O_3 , CeO_2/Al_2O_3 and $Ce_{0.9}Eu_{0.1}O_2/Al_2O_3$ respectively.

The platinum catalyst was prepared in a similar way by wetness impregnation of the targeted Pt loading of 2 wt.% and using tetrammonium nitrate platinate (Johnson Matthey) as metal precursor. As catalyst support a commercial Puralox CeO_2/Al_2O_3 (Sasol) was used. After impregnation, the catalyst was dried and calcined at 350°C during 8 h with a heating rate of 5°C min^{-1} . The obtained catalyst was labelled Pt/CeAl.

2.3. Preparation of the structured catalysts

The washcoating method was used to cover the metallic substrate surface with buffer and catalyst layer successively. For this, slurries with adjusted rheological properties were prepared. For all employed solids, prepared suspensions contain 18.14 wt.% of solid, 1.96 wt.% of polyvinylalcohol (PVA) solution (1.5 wt.% in water), 17.65 wt.% of colloidal Al_2O_3 suspension (Nyacol, 20 wt.% in water) and 62.25 wt.% of H_2O . Prior use, all solids were grinded and sieved to particle size lower than $10\text{ }\mu\text{m}$. During the coating process the PVA, was used to facilitate the suspension impregnation by capillarity within the channels meanwhile Al_2O_3 Nyacol helped the stabilization of the catalyst particles in the resulting suspension [23].

The micromonoliths were immersed for 1 min and then removed from suspensions always at a constant rate of 3 cm min^{-1} . Centrifugation combined with air flushing was employed to remove the excess suspension and to avoid the channels obstruction. For the buffer layer the procedure was repeated several times till the desired amount of 300 mg approx. was deposited. The micromonoliths were calcined at 450°C during 4 h at 2°C min^{-1} heating ramp. The remaining suspensions after layer deposition were dried and calcined in the same conditions as micromonoliths and used for comparison with the powder catalysts. The chosen nomenclature for the suspensions were S_Al, S_CeAl and S_CeEuAl, for the suspensions resulting from the buffers based on Al, CeAl and CeEuAl solids, respectively.

Once a homogeneous buffer layer obtained, the catalyst layer was coated in the same proportions and conditions of deposition used for the buffers. Finally, the micromonoliths were calcined at 350°C for 8 h at 2°C min^{-1} heating ramp. The structured catalysts constituted by two layers, buffer and catalyst ones are labelled M_Al, M_CeAl and M_CeEuAl, while the buffer only deposited monoliths are labelled Mb_Al, Mb_CeAl and Mb_CeEuAl ("b" referring to buffer only), respectively. The targeted quantity of catalyst of approx. 300 mg was achieved after successive washcoating steps. The actual achieved amounts are shown in Table 1.

For all layered systems, both buffer and external catalyst layers are maintained constant, the only variation being the chemical composition of the buffer layer. Both layers present similar densities and textural properties (all having at least 80% of γ - alumina) and, for the similar

Table 1
Structured catalyst' characteristics: loading, specific surface area and estimated layer thickness.

	Buffer layer (g)	Catalyst Layer (g)	S_{BET} (m^2/g)	LT (μm)
Mb_Al	0.33	–	189	3.8
Mb_CeAl	0.34	–	174	3.5
Mb_CeEuAl	0.32	–	159	3.5
M_Al	0.34	0.31	220	7.1
M_CeAl	0.38	0.31	167	7.2
M_CeEuAl	0.32	0.31	139	5.4

deposited quantities, similar layer thickness. The layer thickness was estimated using micromonolith total geometrical area, catalyst density and total pore volume (Table 1).

2.4. Characterization technique

The elemental composition of the powder samples (buffers, catalysts and suspensions) was analyzed by X-Ray fluorescence (XRF) spectrometry carried out in an X Panalytical AXIOS PW4400 using Rh tube as a source of radiation. The textural properties were studied by N₂ adsorption-desorption measurements at liquid nitrogen temperature in a Micrometrics ASAP 2010 instrument. Before analysis, the samples were degassed for 2 h at 150 °C in vacuum. For the monoliths, a specially designed homemade sample holder was used allowing the analysis of a whole monolith.

X'Pert Pro PANalytical instrument was used for X-ray diffraction (XRD) analysis. Diffraction patterns were recorded using Cu K α radiation (40 mA, 45 kV) over a 2 θ -range of 10–95° and a position-sensitive detector using a step size of 0.05° and a step time of 240 s.

Scanning electron microscopy (SEM) analysis and adherence test were performed. SEM was carried out on a JEOL 5400 microscope. The adherence of the layer to the substrate was evaluated introducing the monolith in acetone during 30 min under ultrasound treatment and adherence was related to the amount of catalyst lost during the test respect to the initial loading.

FTIR spectra were recorded using THERMO NICOLET Avatar 380 FT-IR Spectrophotometer, equipped with a DTGS detector, spectral resolution of 4 cm^{-1} and 128 accumulated scans. The experiments were performed *in situ* using purpose-made IR cell connected to conventional vacuum adsorption apparatus with residual pressure lower than 10^{-5} mbar. The experiments consisted of water absorption in small doses at room temperature till saturation. After then, the sample was heated to $50\text{ }^{\circ}\text{C}$, cooled down to room temperature and a spectrum was recorded. This procedure repeated also at 100, 150 and $200\text{ }^{\circ}\text{C}$. The changes produced in respect to the initial IR spectrum, before any water addition, were analyzed.

For the H₂O-TPD, the sample underwent water pulses of 500 μ L each at 120 °C using N₂ as vapor carrier until surface saturation. Once the water signal stabilized ($m/z = 18$), the sample was heated up to 600 °C with a 5 °C min⁻¹ heating rate in order to desorb all water species. The outlet gas composition was normalized by the surface area of each sample and analyzed with a mass spectrometer PFEIFFER Vacuum PrismaPlus controlled by Quadera software.

2.5. Catalytic activity

The water gas shift reaction was carried out in a tubular flow reactor at atmospheric pressure. All samples were tested in the 180–350 °C temperature range, with a gas composition of 7% CO, 9% CO₂, 50% H₂ and 30% H₂O (balanced with N₂), used to simulate the outlet of a typical ethanol reformer reactor. Constant space velocity (WHSV) of 80 L g_{cat}⁻¹ h⁻¹ was used for each micromonoliths test. The powder samples (PtCeAl and S-PtCeAl) were tested using sieved solids in the 600–800 µm fraction range. All samples were activated at 350 °C during

2 h in H₂ stream (10 vol.%) prior the WGS reaction measurement. The CO and CO₂ contents were analyzed with an ABB gas analyzer and the activity is expressed in terms of CO conversion.

The effect of feed stream composition on the catalytic activity was also studied at 310 °C. In these experiments, the influence of each species introduced on the feed stream was analyzed maintaining constant the concentration of the other components. The total flow was also kept constant using N₂ to maintain the GHSV. The starting inlet composition was 50% H₂, 7% CO, 3% CO₂ and 30% (v/v) H₂O (N₂ balance). Please note that, in order to widen the compositional variations, the CO₂ concentration was diminished at 3% CO₂ in respect to the initial one (9% CO₂). Thus, for instance, the effect of the CO₂ partial pressure (Fig. 5A) was evaluated employing a feed stream composed by 50% H₂, 7% CO, 30% (v/v) H₂O in which the CO₂ concentration was modified taking values of 0%, 3%, 9% and 11%. Similarly, the H₂ effect (Fig. 5B) was analyzed under a constant feed stream composed by 7% CO, 3% CO₂ and 30% (v/v) H₂O with H₂ concentrations varied at 0%, 20%, 40%, 50% and 54%. In Fig. 5C, the CO effect was evaluated using 50% H₂, 3% CO₂, 30% (v/v) H₂O and 4.5-7-11% CO. Lastly, the H₂O partial pressure is studied under 50% H₂, 7% CO, 3% CO₂ and 15–30-40% (v/v) H₂O (Fig. 5D).

3. Results and discussion

The chemical compositions of catalyst, buffers and their respective suspensions are presented in Table 2. All systems present compositions close to the desired loading, only a minimal loss of CeO₂ component in respect to alumina is observed. Nevertheless, the obtained Ce/Eu molar ratio of 12 instead of 9 in the originally designed solid indicates lower Eu incorporation within the ceria matrix. Compared to the parent initial solids, the changes observed for the suspension chemical compositions could be attributed to the additional alumina component introduced during the slurry preparation. The incorporation of colloidal alumina (Nyacol) increases overall alumina content and hence, automatically decreases ceria, europia and platinum loadings, as reflected in Table 2.

The textural properties of buffer solids, catalyst and respective suspensions are also shown in Table 2. All solids are mesoporous with specific surface area dominated by the presence of alumina. Among initial buffer solids, the pure alumina buffer sample presents the highest specific surface area diminishing respectively with CeO₂ and/or Ce-Eu mixed oxide addition. In comparison to the corresponding bare solids, the textural properties of the suspensions are furthermore modified by the presence of Nyacol (192 m²/g; 0.58 cm³/g) as reflected in their higher specific surface areas and pore volumes.

All structured catalyst presented the same catalyst layer amount (Table 1). However, some slight differences are found for the buffer layer loadings between the samples. As for the powder samples, the structured ones containing alumina buffer layers (Mb_Al and M_Al) present the highest specific surface area which decrease with the addition of bare or mixed ceria oxide. No direct correlations have been found regarding the specific surface area minor variations between the micromonoliths and the suspensions. Meanwhile the Mb Al and M Al

Table 2
Chemical composition and textural properties of the powder samples in wt. %.

	Al ₂ O ₃ (wt.%)	CeO ₂ (wt.%)	Eu ₂ O ₃ (wt.%)	Pt (wt.%)	Area (m ² g ⁻¹)	V _{pore} (cm ³ g ⁻¹)
Al	100	–	–	–	169	0.38
S_ Al	100	–	–	–	178	0.37
CeAl	77.4	24.6	–	–	133	0.28
S_ CeAl	82.1	17.9	–	–	177	0.32
CeEuAl	80.8	16.4	2.8	–	132	0.29
S_ CeEuAl	82.2	15.7	2.1	–	166	0.36
Pt/CeAl	75.6	21.8	–	2.6	142	0.30
S_ Pt/CeAl	80.7	17.3	–	2.0	156	0.34

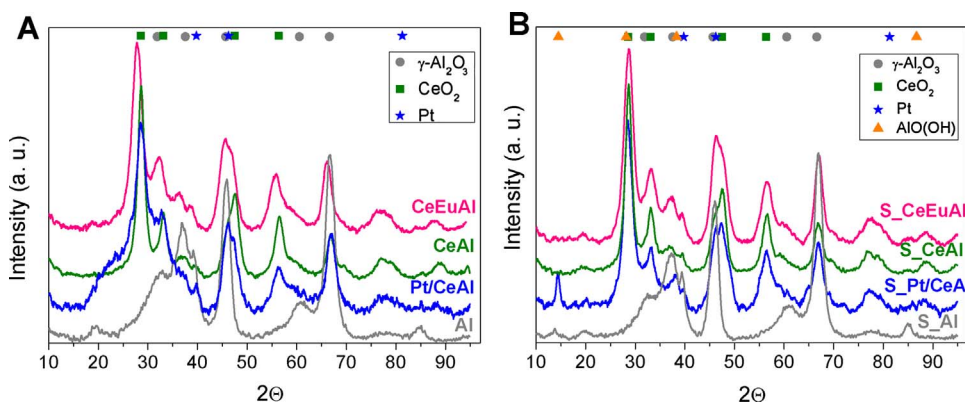


Fig. 2. XRD of the powder samples: A) Al, CeAl, CeEuAl and Pt/CeAl; B) S_Al, S_CeAl, S_CeEuAl and S_Pt/CeAl.

specific surface areas increased in comparison to S_Al, those of Mb(M)_CeAl and Mb(M)_CeEuAl decreased compared to their respected suspension. Lower resistances against thermal sintering of the ceria based solids could account for the observed differences.

The XRD patterns of all powder samples are shown in Fig. 2. Al, CeAl, CeEuAl and Pt/CeAl samples present all diffraction lines corresponding to CeO_2 fluorite (JCPDS# 00-004-0593) and $\gamma\text{-Al}_2\text{O}_3$ (JCPDS# 00-048-0267) structures. In the case of CeEuAl, no diffraction lines due to crystalline europium oxide are detected. Moreover, the observed slight shifts in the CeO_2 main diffraction peaks respect to those of CeAl indicate the formation of Ce-Eu mixed oxide. The calculation of the ceria lattice parameter, using the (111) main plane diffraction, shows an increase of the parameter value from 5.39 Å for CeAl to 5.40 Å for CeEuAl sample accounting for partial Ce^{4+} substitution by Eu^{3+} ions. This substitution confirms the solid solution formation and implies also the appearance of oxygen vacancies obtained by charge compensation mechanism (Ce^{4+} is substituted by greater ion with lower charge Eu^{3+}). The lattice distortion also results in smaller CeO_2 crystal size, as estimated by Scherrer's equation, 38 nm for CeEuAl vs. 55 nm for CeAl. This fact could be attributed completely to the lattice alteration, produced by europium insertion, after which the crystal growth is restricted, resulting in smaller crystal domains. No diffractions attributed to Pt are observed for Pt/CeAl sample suggesting high dispersion of the noble metal with crystalline domains under the detection limit of the technique (5 nm).

No important differences of suspension's XRD patterns (Fig. 2B) with respect to their parent solids are detected. The latter indicates the absence of solid structural changes during suspension preparation procedure. Still, the appearance of new alumina boehmite phase (JCPDS# 00-21-1307) corresponding to that issued from Nyacol is identified for the Pt/CeAl probably related to the lower calcination temperature in comparison to the buffer solids.

The adherence test on the micromonolithic series indicates an excellent adherence with 94–97% catalyst layer remaining after the test. In all cases, the SEM micrographs confirm the presence of well-dispersed homogeneous catalytic layers as shown in Fig. 3A representing selected micrograph obtained for M_CeAl monolith and its corresponding cross section micrograph including the line analysis (Fig. 3B). From left to right, three layers can be distinguished: i) the metallic substrate characterized by Fe-Cr presence; ii) a layer constituted by alumina produced during the thermal pretreatment of the monolith steel, the colloidal Al_2O_3 added during to the slurry preparation and the alumina component coming from the buffer itself and iii) an external surface layer rich in CeO_2 .

The powder Al, CeAl and CeEuAl samples, their corresponding suspensions (S_Al, S_CeAl and S_CeEuAl) and buffer only micromonoliths (Mb_Al, Mb_CeAl and Mb_CeEuAl) do not present catalytic activity at the employed temperature and gas mixture conditions. The bare catalysts powder and suspensions (Pt/CeAl and S_Pt/CeAl) do not differ in activity indicating that the catalyst properties are not

influenced by the catalyst to suspension switch operation (data not shown). In addition, the estimated layer thickness of a maximum of 7 μm (Table 1), indicates an effectiveness factor close to 1 for which the diffusional phenomena controlling the reaction can be ruled out [2,25,26]. Thus, all differences in activity for the multilayered samples will be related to the buffer layer nature. The catalytic activity of all structured systems is shown in Fig. 4A. None of the catalysts achieves CO equilibrium conversion (Fig. 4A), probably due to the exigent operational conditions employed in this study, i.e. low contact time and high H_2 and CO partial pressures. Similarly, Kolb et al. [27] reported CO conversions below 30% at 310 °C employing similar feed streams and catalyst composition. Also, Germani et al. [28] presented comparable catalytic behavior for comparable feed stream composition and catalysts. The activity tendency in CO conversion terms obeys the following order: M_Al < M_CeAl < M_CeEuAl. The activity trend is even more accentuated under normalization of the converted CO molecules over the overall specific surface area exposed to the reactants (Fig. 4B). It is clear that the addition of ceria to alumina greatly improves the catalytic activity, improved even more with europium to ceria doping. One can postulate that the observed activity improvement is directly related to the concentration of oxygen vacancies during the reaction in a way that the higher the vacancies number, the higher the WGS activity. In addition, the covalency of the Ce-O bond is affected by the presence of Eu resulting in different capacity for facing up water dissociation process, i.e. different H/OH surface coverages from water dissociative reactions within solids oxygen vacancies.

The behavior of the micromonoliths as a function of buffer nature under different reaction atmospheres was also studied. In order to broaden the compositional range, the initial feed was slightly altered by reducing the CO_2 concentration (7% CO + 3% CO_2 + 50% H_2 + 30% H_2O). This allows performing the composition variation study (one per experiment) under similar conditions. The observed activity variation is reflected in Fig. 5.

No substantial changes upon CO_2 concentration variation are observed. In fact, no important activity diminutions are observed until high CO_2 concentrations in the feed stream are introduced being the resistance versus the CO_2 species emphasized for both the ceria containing buffers. On the contrary, a notorious CO conversion decrement decrease was observed when increasing the hydrogen concentration. Considering that the WGS reaction is an equilibrium reaction, the incorporation of both products (CO_2 or H_2) should lead to a decrease in CO conversions in both cases. Therefore, while a strong inhibition is detected from H_2 species, CO_2 molecules could be just considered as negative at higher gas concentrations. In very good agreement with the observed trends, for similar conditions and catalytic systems, kinetic equations with CO_2 and H_2 partial kinetic orders of 0 and -0.5 respectively, are proposed in literature [28,29].

The increment of CO concentration on the feed stream also entails a decrement of the CO conversions, related to the increase of the number of CO molecules, which have to be converted by the same number of

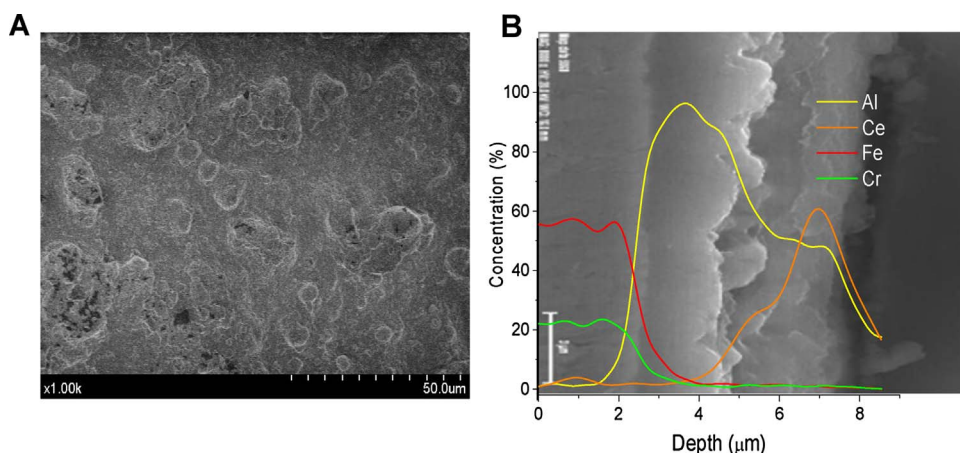


Fig. 3. SEM microphotographs of Mb_CeAl A) front image; B) cross section overlapped with line analysis.

active sites. Besides, the catalytic inhibition should be also related to the competitive CO-H₂O absorptions over the active sites: Pt and Pt/Ceria interfaces. This means that, at higher CO coverages, the available OH population surrounding the active sites should decrease and, as a direct consequence, lead to lower CO conversions [30]. For those three components, the changes provoked by the feed variations remain within the same magnitude no matter the buffer nature and no important differences are observed. Besides and as expected, the ceria containing samples always present higher CO conversions.

The increase of H₂O concentration (Fig. 5D), however, involves significant changes in the catalyst WGS behavior. At low water concentrations, all micromonoliths present the same conversion values gradually increasing with water enrichment of the feed. Since the WGS is an equilibrium, an enhancement of the activity with the water partial pressure rise is expected but this improvement appears to depend on the buffer's composition following the sequence: M_CeEuAl > M_CeAl > M_Al. Therefore, the sequence of activity correlates with the increasing oxygen vacancies concentration which favors and makes easier the water activation. The presence of buffer layer, associated to the existence of extra number of defect sites, results in changed electronic properties and influences the reactants coverages on the catalyst surface [25]. From the improved capacity for dissociating water, an increase of the OH/H species population near the active Pt sites could be related to the enhanced catalytic behaviors. According to the initial hypothesis, water activation capacity and consequent catalytic behavior can be modulated by the buffers composition in a way that the higher the number ceria defects, the higher the water activation rate and the higher the activity.

The relationship between H₂O surface interactions and the buffer nature was evaluated by Infrared spectroscopy. In general, the introduction of certain water quantities to the system could lead either to water adsorption and/or to water dissociation. The Fig. 6 presents the

hydroxyl band evolution for the S_Al, S_CeAl and S_CeEuAl samples during successive water introduction steps. The important alumina content in all the samples explains the observed similar spectra. For all the samples, the evolution of the 1764–1414 cm⁻¹ region when introducing water is also shown in Fig. 6D. Weak bands placed at about 1640–1595 cm⁻¹ accounts for water molecularly adsorbed within different chemical environments, δ(HOH) [31]. For S_Al (Fig. 6A), different bands corresponding to hydroxyl species adsorbed on alumina surface and placed at 3781, 3734, 3692, 3580 and 3532 cm⁻¹ dominates the spectrum. The first three bands are generally attributed to OH groups bounded mono or bicoordinated to tetrahedrally Al³⁺ species [32–34] and the last two ones (3580 and 3532 cm⁻¹) are typical for H-bonded to OH species or non-dissociated water molecules [31,35]. Successive water adsorptions clearly lead to 3734 cm⁻¹ band intensity diminutions along with intensity increments of the molecularly water absorbed related bands (3580, 3532 and 1640 cm⁻¹). Besides, the water doses entail very tiny increments of the 3781 and 3692 cm⁻¹ OH bands indicating the minor water dissociation capacities characteristic of Al₂O₃ surfaces. In turn, in absence of important dissociative processes, increasing amounts of molecularly absorbed water species should provoke a decrease of the hydroxyl band intensity since the O–H bond strength will become weaker because of the OH – H₂O dipole formation and interaction. Despite that a slight Al₂O₃ surface capacities for dissociating water molecules cannot be completely ruled out, in agreement to the clear observed features the water introduction over S_Al sample principally entails molecular water absorptions.

For S_CeAl (Fig. 6B), bands placed at 3777, 3731, 3687, 3580 and 3514 cm⁻¹ are observed. As expected, some differences are detected on the band positions in respect to the initial Al bands accounting mainly for ceria presence and surface-water modified interactions. For instance, the OH band at 3781 cm⁻¹ showed by the S_Al sample is shifted to 3777 cm⁻¹ in the S_CeAl one owing to different chemical

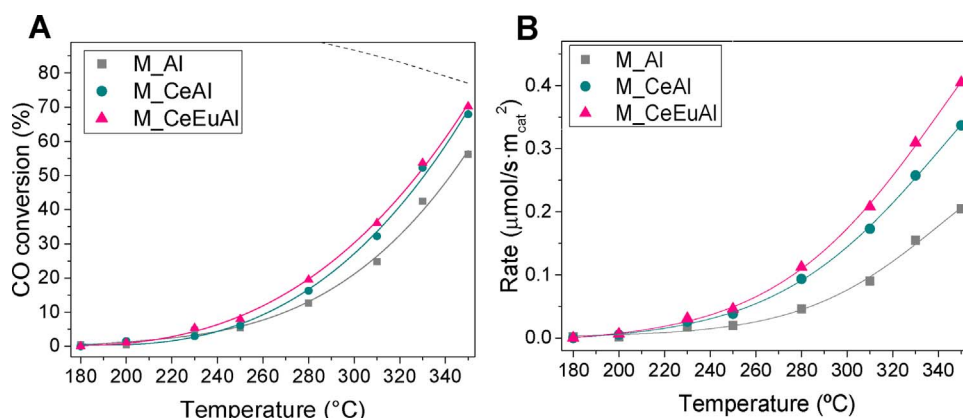


Fig. 4. Catalytic activity at 80 L g⁻¹ h⁻¹ and employing 7% CO, 9% CO₂, 30% H₂O, 50% H₂ as feed: A) CO conversions; B) Rate. (Equilibrium curve: dashed line).

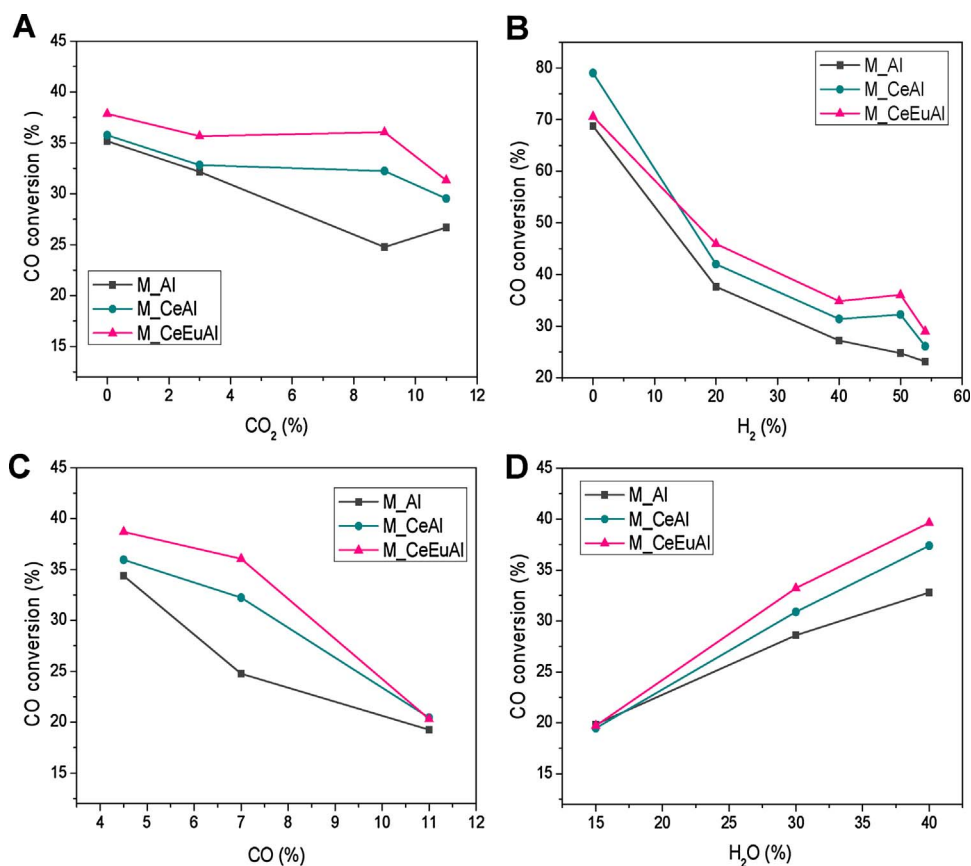


Fig. 5. CO conversion of M_Al, M_CeAl and M_CeEuAl catalysts as a function of concentration of: A) % CO₂; B) % H₂; C) % CO and D) % H₂O. T = 310 °C.

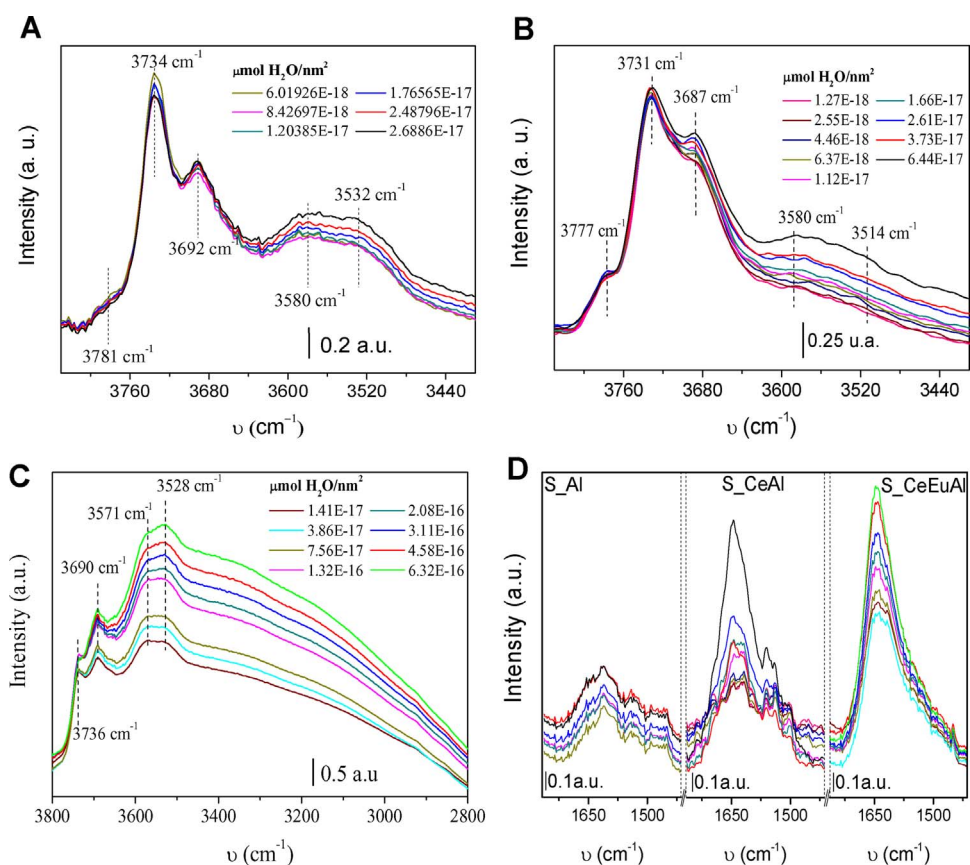


Fig. 6. FT-IR spectra upon water absorption for: A) S_Al; B) S_CeAl; C) S_CeEuAl; D) Corresponding band evolution on the 1764–1414 cm⁻¹ region exhibited for each sample during the water absorption tests.

environments provoked from the cerium oxide incorporation. Also, the S_{Al} band placed at 3734 cm^{-1} is also slightly shifted to lower wavelengths, probably due to the low intensity cerium oxide band reported at 3710 cm^{-1} being attributed to OH(I) species adsorption [31]. The band situated at 3687 cm^{-1} is related to OH species on Ce^{3+} or Ce^{4+} atoms [35]. Again, the bands at ca. 3580 and 3514 cm^{-1} are associated to undissociated water molecules [32,35,36]. Subsequent water pulses entail superior Ce-OH band intensities (3731 and 3687 cm^{-1}) suggesting the ceria surface ability for dissociating water species. The noticeable increment observed for the band at ca. 3687 cm^{-1} suggests its relation to Ce^{3+} defective sites with its corresponding ability for dissociate water species. The S_{CeAl} system, in comparison to the S_{Al} one, exhibits more pronounced intensity growths on the bands associated to absorbed water molecules (3580 , 3514 and 1640 cm^{-1}) indicating that defective ceria surfaces also display higher water absorption capacities.

S_{CeEuAl} sample upon water adsorption presents bands situated at 3736 , 3690 , 3571 and 3528 cm^{-1} , respectively. An additional shift of the bands position is observed and could be correlated to different chemical environments achieved upon europium insertion into ceria lattice. No bands of europium oxide – H₂O interaction are detected. The successive water introduction involves higher OH population (3736 and 3690 cm^{-1}) on the S_{CeEuAl} surface. Also, strongly pronounced band intensity raises are observed for the bands placed at 3571 , 3528 and 1640 cm^{-1} evidencing its remarked water adsorption capacity. In parallel, the noticeably wide band at the $3490\text{--}2800\text{ cm}^{-1}$ range could be also directly related to higher absorbed water quantities.

Therefore, the determining role of the surface composition on the water dissociation capacities is clearly established from the OH band evolution as a function of the water partial pressures. The direct relationship between the water splitting ability and the oxygen vacancy population is evidenced since: the higher the oxygen vacancies concentration, the higher the water splitting capacity. This water dissociation promotion could be explained considering the electrons intrinsically associated to the oxygen vacancies, $\text{Ce}^{3+}\text{--Ov}^{\bullet}$. As a consequence, superior oxygen defect surface populations should lead to higher electronic densities which entail shifted Fermi's level through favored electron delocalization processes and enhanced water reduction reactions [37,38]. Then, an intimate relationship between OH surface populations, water splitting capacity and catalytic performances could be established [9,39]. For Pt based catalysts, Petallidou et al. [40] related superior WGS reaction rates to higher Ov concentration and H and C containing intermediates on the Pt-support interface. In agreement, employing FT-IR and TPD studies, we have demonstrated that improved catalytic behaviors were related to enhanced H₂-reducibilities which entail superior carbonaceous species developed on the catalytic surface [9]. Despite it is not explicitly showed in this manuscript, it should be noted that the greater surface concentration of H/OH, achieved by the Ov promotion, should also involve boosted surface dynamics concerning not only to H-containing but also C-containing intermediates.

On the other hand, interesting outcomes could also be extracted from Fig. 7 where the spectra of the different samples are displayed when equal water amounts ($3\cdot 10^{-18}\text{ }\mu\text{mol}/\text{nm}^2$) are introduced. Not only the dissociated water species but also the amount of water molecules absorbed on the surface respond to the following sequence: S_{CeEuAl} > S_{CeAl} > S_{Al}. It is worth highlighting the band placed at 2137 cm^{-1} uniquely noted by the S_{CeEuAl} sample. In literature, a band situated at about 2120 cm^{-1} has been attributed to forbidden $^2\text{F}_{5/2} \rightarrow ^2\text{F}_{7/2}$ transition and associated Ce^{3+} species present on defective ceria surfaces [31,41]. Most probably, the difference between both band positions could be attributed to different chemical environments motivated by the Eu presence. The Eu species on the Ov surroundings will markedly affect the chemical environment of the oxygen vacancies and then, the band position associated to Ce^{3+} species. Thus, S_{CeEuAl} sample absorbs the highest amount of water on its surface at the same

time as it presents the greatest water dissociative capacity. Hence, the oxygen defects concentration strongly influences the surface chemisorptive properties and results in modulated OH/H₂O surface interactions and consequently, modulated surface coverages and catalytic behaviors [9].

After water saturation, the samples were degassed first by applying different pressures (ϕ_1 , ϕ_2) and, then by heating to $T = 50$, 100 , 150 and $200\text{ }^{\circ}\text{C}$. For the $1780\text{--}1400\text{ cm}^{-1}$ region, the spectra obtained during the water desorption process for S_{CeAl} and S_{CeEuAl} are shown in Fig. 8A. Apart from the described correlation between the oxygen vacancies population and the amount of water molecules absorbed, the surface defect concentration also affects the absorption water strength since S_{CeEuAl} presents higher amounts of absorbed water at the different temperatures evaluated during the desorption process.

The oxygen vacancies effect on the water surface interactions were also evaluated by H₂O-TPD experiments over the S_{Al}, S_{CeAl} and S_{CeEuAl} powder samples after surface saturation with successive water vapor pulses. The observed changes in this experiment should account for the different type of water surface interactions as a function of support nature. The $m/z = 18$ profile under H₂O-TPD conditions is presented in Fig. 8B with the WGS temperature range ($0\text{--}350\text{ }^{\circ}\text{C}$) amplified. The desorptive profiles of the samples are composed by two main desorption zones as a function of the temperature: $120\text{--}350\text{ }^{\circ}\text{C}$ and $350\text{--}600\text{ }^{\circ}\text{C}$. The highest temperature desorption zone can be tentatively attributed to processes related to alumina presence at around $500\text{ }^{\circ}\text{C}$ and to the OH groups lost at temperatures around $600\text{ }^{\circ}\text{C}$. The desorption processes observed at lower temperature could be ascribed, in temperature ascending order, to physically adsorbed water at temperatures below $200\text{ }^{\circ}\text{C}$ and to desorption of water adsorbed on ceria surfaces for temperatures above $200\text{ }^{\circ}\text{C}$. For ceria based samples, similar experimental H₂O-TPD profiles were reported by Thion et al. [42]. According to their simulations, based on the kinetic law proposed by Germani et al. [28], the two main desorption processes at $120\text{ }^{\circ}\text{C}$ and $260\text{ }^{\circ}\text{C}$ should be respectively attributed to molecular and dissociative water desorptions.

Therefore, the S_{Al} desorption profile shows water desorptions earlier than in both ceria samples corroborating the stronger water interactions attained through the ceria incorporation. Besides, the low water amount desorbed at about $220\text{ }^{\circ}\text{C}$ suggests the tiny capacity for water splitting of Al₂O₃ surfaces. Also, the higher absorptive and dissociative capacities detected for both ceria samples are again underlined by the larger overall desorptive processes exhibited by those samples being much greater than those showed by the S_{CeEuAl}. The preferred water adsorptions over reduced ceria surfaces, more precisely, over Ce^{3+} sites associated to oxygen defects in pure ceria lattices account for the observed features [43]. The higher contribution discerned for the ceria based samples at about $260\text{ }^{\circ}\text{C}$ unequivocally ratifies the connection between oxygen vacancies populations with the superior water surface interaction strengths and also, with the enhanced water dissociative abilities. Therefore, the proposed catalytic activity sequence: M_{CeEuAl} > M_{CeAl} > M_{Al}, which suits to the oxygen vacancies concentration within the inner layer of the structured catalysts, could be also extended to the different system abilities for interacting to the water species in terms of absorption, dissociation and interacting strength.

4. Conclusions

The confluence of the benefits provided by the use of metallic micromonolith and the multilayer approach for the WGS activity has been merged and deeply evaluated. The structured catalyst design includes the development of an innovative multilayered catalyst composed by an external PtCeAl catalyst and an internal buffer layer with varied chemical composition. The latter is finely tuned considering water dissociation as the reaction limiting step and the role of the oxygen defects concentration on it. The catalytic activity results evidenced that the

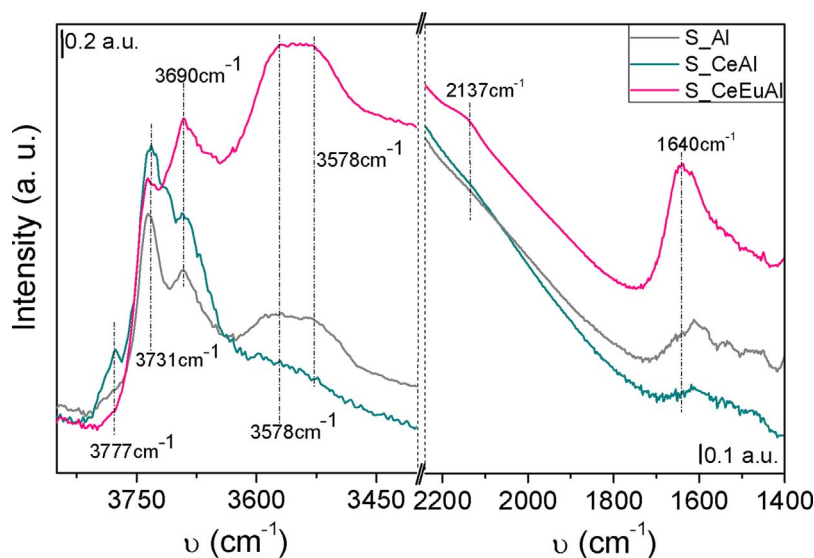


Fig. 7. FT-IR spectra obtained when $3 \cdot 10^{-17}$ $\mu\text{mol}/\text{nm}^2$ water were absorbed for S_Al, S_CeAl and S_CeEuAl for the $3850\text{--}3400\text{ cm}^{-1}$ and $2240\text{--}1400\text{ cm}^{-1}$ regions, respectively.

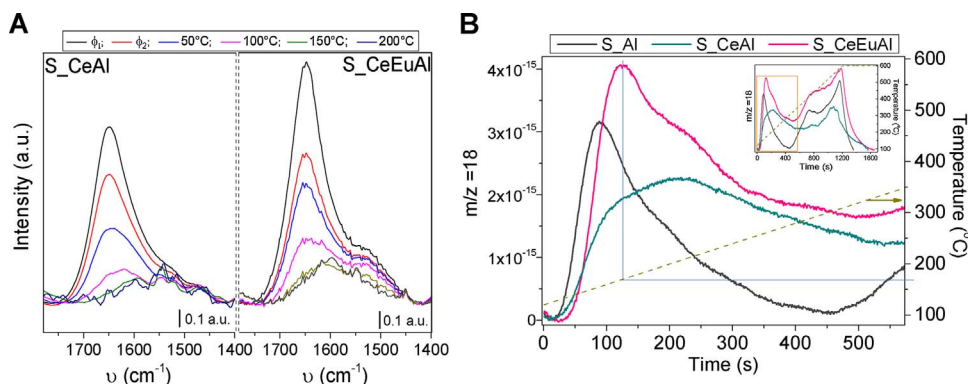


Fig. 8. A) FT-IR spectra obtained on the $1780\text{--}1400\text{ cm}^{-1}$ region during the water desorption experiment for the S_CeAl and S_CeEuAl samples; B) H_2O -TPD obtained for the S_Al, S_CeAl and S_CeEuAl samples.

catalyst behavior is modulated by the buffer layer composition or, more precisely, by the increase of the number of oxygen vacancies. A superior oxygen vacancies concentration provokes higher electron densities and entails boosted water reductive abilities. Remarkably, in view of the FT-IR and H_2O -TPD results, the defect surface concentration not only determines the dissociative water reactions by itself but also defines the molecular water interactions with the surface. The ensuing better abilities to absorb, maintain and dissociate the surface water species results on changed surface coverages, rising up the apparent partial H_2O pressures and consequences on WGS catalytic improvements.

As a result, the multilayered concept for obtaining superior WGS catalytic performance is validated and intimately related to the changes on the water surface interactions. The proposed novel design for WGS structured catalysts appears as a potent strategy able to tailor the behavior of a standard WGS catalysts.

Acknowledgments

Financial support for this work has been obtained from the Spanish Ministry of Economy and Competitiveness (ENE2015-66975-C3-2-R) and from Junta de Andalucía (TEP-8196), both co-financed by FEDER funds from the European Union.

References

- [1] C. Ratnasamy, J.P. Wagner, Water gas shift catalysis, *Catal. Rev.* 51 (2009) 325–440, <http://dx.doi.org/10.1080/01614940903048661>.
- [2] R.J. Farrauto, Y. Liu, W. Ruettinger, O. Ilinich, L. Shore, T. Giroux, Precious metal catalysts supported on ceramic and metal monolithic structures for the hydrogen economy, *Catal. Rev.* 49 (2007) 141–196, <http://dx.doi.org/10.1080/01614940701220496>.
- [3] W. Ruettinger, O. Ilinich, R.J. Farrauto, A new generation of water gas shift catalysts for fuel cell applications, *J. Power Sources* 118 (2003) 61–65, [http://dx.doi.org/10.1016/S0378-7753\(03\)00062-4](http://dx.doi.org/10.1016/S0378-7753(03)00062-4).
- [4] D.C. Grenoble, M.M. Estadt, D.F. Ollis, The chemistry and catalysis of the water gas shift reaction. 1. The kinetics over supported metal catalysts, *J. Catal.* 67 (1981) 90–102, [http://dx.doi.org/10.1016/0021-9517\(81\)90263-3](http://dx.doi.org/10.1016/0021-9517(81)90263-3).
- [5] S. Damyanova, J.M. Bueno, Effect of CeO₂ loading on the surface and catalytic behaviors of CeO₂-Al₂O₃-supported Pt catalysts, *Appl. Catal. A Gen.* 253 (2003) 135–150, [http://dx.doi.org/10.1016/S0926-860X\(03\)00500-3](http://dx.doi.org/10.1016/S0926-860X(03)00500-3).
- [6] A. Holmgren, B. Andersson, D. Duprez, Interactions of CO with Pt/ceria catalysts, *Appl. Catal. B Environ.* 22 (1999) 215–230, [http://dx.doi.org/10.1016/S0926-3373\(99\)00047-8](http://dx.doi.org/10.1016/S0926-3373(99)00047-8).
- [7] T. Ramírez Reina, M. González Castaño, S. Palma, S. Ivanova, J.A. Odriozola, Twenty years of golden future in the water gas shift reaction, *Heterog. Gold Catal. Catal.* (2014) 111–139, <http://dx.doi.org/10.1039/9781782621645-00111>.
- [8] M. González Castaño, T.R. Reina, S. Ivanova, M.A. Centeno, J.A. Odriozola, Pt vs. Au in water-gas shift reaction, *J. Catal.* 314 (2014) 1–9, <http://dx.doi.org/10.1016/j.jcat.2014.03.014>.
- [9] M. González-Castaño, S. Ivanova, T. Ioannides, M.A. Centeno, J.A. Odriozola, Deep insight into Zr/Fe combination for successful Pt/CeO₂/Al₂O₃ WGS catalyst doping, *Catal. Sci. Technol.* 7 (2017) 1556–1564, <http://dx.doi.org/10.1039/C6CY02551J>.
- [10] A. Trovarelli, Catalytic properties of ceria and ceria-containing materials, *Catal. Rev.* 38 (1996) 439–520, <http://dx.doi.org/10.1016/j.nima.2005.07.053>.
- [11] A. Trovarelli, C. de Leitenburg, M. Boaro, G. Dolcetti, The utilization of ceria in industrial catalysis, *Catal. Today* 50 (1999) 353–367, [http://dx.doi.org/10.1016/S0920-5861\(98\)00515-X](http://dx.doi.org/10.1016/S0920-5861(98)00515-X).
- [12] C.M. Kalamaras, K.C. Petalidou, A.M. Efstathiou, The effect of La³⁺-doping of CeO₂ support on the water-gas shift reaction mechanism and kinetics over Pt/Ce_{1-x}La_xO_{2-δ}, *Appl. Catal. B Environ.* 136–137 (2013) 225–238, <http://dx.doi.org/10.1016/j.apcatb.2013.02.003>.
- [13] T.R. Reina, W. Xu, S. Ivanova, M. Á. Centeno, J. Hanson, J. a. Rodriguez, J.A. Odriozola, In situ characterization of iron-promoted ceria-alumina gold catalysts during the water-gas shift reaction, *Catal. Today* 205 (2013) 41–48, <http://dx.doi.org/10.1016/j.cattod.2012.08.004>.
- [14] T. Tabakova, V. Idakiev, D. Andreeva, I. Mitov, Influence of the microscopic properties of the support on the catalytic activity of Au/ZnO, Au/ZrO₂, Au/Fe₂O₃, Au/Fe₂O₃-ZnO, Au/Fe₂O₃-ZrO₂ catalysts for the WGS reaction, *Appl. Catal. A*

- Gen. 202 (2000) 91–97, [http://dx.doi.org/10.1016/S0926-860X\(00\)00463-4](http://dx.doi.org/10.1016/S0926-860X(00)00463-4).
- [15] T. Tabakova, L. Ilieva, I. Ivanov, R. Zanello, J.W. Sobczak, W. Lisowski, Z. Kaszkur, D. Andreeva, Influence of the preparation method and dopants nature on the WGS activity of gold catalysts supported on doped by transition metals ceria, *Appl. Catal. B Environ.* 136–137 (2013) 70–80, <http://dx.doi.org/10.1016/j.apcatb.2013.01.050>.
- [16] A. Holmgren, B. Andersson, Oxygen storage dynamics in Pt/CeO₂/Al₂O₃ catalysts, *J. Catal.* 25 (1998) 14–25.
- [17] W.Y. Hernández, M.A. Centeno, F. Romero-Sarria, J.A. Odriozola, Synthesis and characterization of Ce_{1-x}Eu_xO_{2-x/2} mixed oxides and their catalytic activities for CO oxidation, *J. Phys. Chem. C* 113 (2009) 5629–5635.
- [18] W.Y. Hernández, O.H. Laguna, M.A. Centeno, J.A. Odriozola, Structural and catalytic properties of lanthanide (La, Eu, Gd) doped ceria, *J. Solid State Chem.* 184 (2011) 3014–3020, <http://dx.doi.org/10.1016/j.jssc.2011.09.018>.
- [19] G. Kolb, V. Hessel, Micro-structured reactors for gas phase reactions, *Chem. Eng. J.* 98 (2004) 1–38, <http://dx.doi.org/10.1016/j.cej.2003.10.005>.
- [20] M. González-Castaño, T.R. Reina, S. Ivanova, L.M. Martínez Tejada, M.A. Centeno, J.A. Odriozola, O₂-assisted water gas shift reaction over structured Au and Pt catalysts, *Appl. Catal. B Environ.* 185 (2016) 337–343, <http://dx.doi.org/10.1016/j.apcatb.2015.12.032>.
- [21] A.S. Quiney, G. Germani, Y. Schuurman, Optimization of a water–gas shift reactor over a Pt/ceria/alumina monolith, *J. Power Sources* 160 (2006) 1163–1169, <http://dx.doi.org/10.1016/j.jpowsour.2006.03.019>.
- [22] P. Avila, M. Montes, E.E. Miró, Monolithic reactors for environmental applications, *Chem. Eng. J.* 109 (2005) 11–36, <http://dx.doi.org/10.1016/j.cej.2005.02.025>.
- [23] L.M. Martínez Tejada, M.I. Domínguez, O. Sanz, M.A. Centeno, J.A. Odriozola, Au/CeO₂ metallic monolith catalysts: influence of the metallic substrate, *Gold Bull.* 46 (2013) 221–231, <http://dx.doi.org/10.1007/s13404-013-0102-0>.
- [24] O. Sanz, T.F.J. Martínez T, F.J. Echave, M.I. Domínguez, M.A. Centeno, J.A. Odriozola, M. Montes, Aluminium anodisation for Au-CeO₂/Al₂O₃-Al monoliths preparation, *Chem. Eng. J.* 151 (2009) 324–332, <http://dx.doi.org/10.1016/j.cej.2009.03.062>.
- [25] M. González-Castaño, S. Ivanova, O.H. Laguna, L.M. Martínez T, M.A. Centeno, J.A. Odriozola, Structuring Pt/CeO₂/Al₂O₃ WGS catalyst: introduction of buffer layer, *Appl. Catal. B Environ.* 200 (2017) 420–427, <http://dx.doi.org/10.1016/j.apcatb.2016.07.039>.
- [26] D.I. Potemkin, P.V. Snytnikov, V.D. Belyaev, V.A. Sobyanin, Preferential CO oxidation over Cu/CeO₂-x catalyst: internal mass transport limitation, *Chem. Eng. J.* 176–177 (2011) 165–171, <http://dx.doi.org/10.1016/j.cej.2011.08.081>.
- [27] G. Kolb, H. Pennemann, R. Zapf, Water-gas shift reaction in micro-channels—results from catalyst screening and optimisation, *Catal. Today* 110 (2005) 121–131, <http://dx.doi.org/10.1016/j.cattod.2005.09.012>.
- [28] G. Germani, P. Alphonse, M. Courty, Y. Schuurman, C. Mirodatos, Platinum/ceria/alumina catalysts on microstructures for carbon monoxide conversion, *Catal. Today* 110 (2005) 114–120, <http://dx.doi.org/10.1016/j.cattod.2005.09.017>.
- [29] T. Salmi, R. Hakkarainen, Kinetic study of the low-temperature water-gas shift reaction over a CuZnO catalyst, *Appl. Catal.* 49 (1989) 285–306, [http://dx.doi.org/10.1016/S0166-9834\(00\)83024-9](http://dx.doi.org/10.1016/S0166-9834(00)83024-9).
- [30] N. Guo, B.R. Fingland, W. Damion Williams, V.F. Kispersky, J. Jelic, W.N. Delgass, F.H. Ribeiro, R.J. Meyers, J.T. Miller, Determination of CO, H₂O and H₂ coverage by XANES and EXAFS on Pt and Au during water gas shift reaction, *Phys. Chem. Chem. Phys.* 12 (2010) 5678–5693, <http://dx.doi.org/10.1039/b926434e>.
- [31] C. Binet, M. Daturi, J. Lavalley, O.À. Superoxide, IR study of polycrystalline ceria properties in oxidised and reduced states, *Catal. Today* 50 (1999) 207–225, [http://dx.doi.org/10.1016/S0920-5861\(98\)00504-5](http://dx.doi.org/10.1016/S0920-5861(98)00504-5).
- [32] M.I. Zaki, M.A. Hasan, F.A. Al-Sagheer, L. Pasupulety, In situ FTIR spectra of pyridine adsorbed on SiO₂-Al₂O₃, TiO₂, ZrO₂ and CeO₂: general considerations for the identification of acid sites on surfaces of finely divided metal oxides, *Colloids Surf. A Physicochem. Eng. Asp.* 190 (2001) 261–274, [http://dx.doi.org/10.1016/S0927-7757\(01\)00690-2](http://dx.doi.org/10.1016/S0927-7757(01)00690-2).
- [33] A. Davydov, *Molecular Spectroscopy of Oxide Catalyst*, (2003).
- [34] P. Nortier, P. Fourre, A.B. Mohammed, J.C. Lavalley, Effects of crystallinity and morphology on the surface properties of alumina, *Appl. Catal.* 61 (1990) 141–160.
- [35] P. Bazin, O. Saur, J.C. Lavalley, M. Daturi, G. Blanchard, FT-IR study of CO adsorption on Pt/CeO₂: characterisation and structural rearrangement of small Pt particles, *Phys. Chem. Chem. Phys.* 7 (2005) 187–194, <http://dx.doi.org/10.1039/b414159h>.
- [36] A. Badri, C. Binet, J. Lavalley, An FTIR study of surface ceria hydroxy groups during a redox process with H₂, *J. Chem. Soc. Faraday Trans.* 92 (1996) 4669–4673.
- [37] N. Acerbi, S. Golunski, S.C. Tsang, H. Daly, C. Hardacre, R. Smith, P. Collier, Promotion of ceria catalysts by precious metals: changes in nature of the interaction under reducing and oxidizing conditions, *J. Phys. Chem. C* 116 (2012) 13569–13583, <http://dx.doi.org/10.1021/jp22233u>.
- [38] Z.V. Popović, Z.D. Dohčević-Mitrović, N. Paunović, M. Radović, Evidence of charge delocalization in Ce_{1-x}Fe_xO₂ + (3 + x)/O_{2-y} nanocrystals (x = 0, 0.06, 0.12), *Phys. Rev. B Condens. Matter Mater. Phys.* 85 (2012) 1–6, <http://dx.doi.org/10.1103/PhysRevB.85.014302>.
- [39] C.M. Kalamaras, D.D. Dionysiou, A.M. Efstathiou, Mechanistic studies of the Water–Gas shift reaction over Pt/CeZr_{1-x}O₂ catalysts: the effect of Pt particle size and Zr dopant, *ACS Catal.* 2 (2012) 2729–2742, <http://dx.doi.org/10.1021/cs3006204>.
- [40] K.C. Petalidou, C.M. Kalamaras, A.M. Efstathiou, The effect of La³⁺, Ti⁴⁺ and Zr⁴⁺ dopants on the mechanism of WGS on ceria-doped supported Pt catalysts, *Catal. Today* 228 (2014) 183–193, <http://dx.doi.org/10.1016/j.cattod.2013.10.081>.
- [41] T. Tabakova, M. Manzoli, F. Vindigni, V. Idakiev, F. Boccuzzi, CO-free hydrogen production for fuel cell applications over Au/CeO₂ catalysts: FTIR insight into the role of dopant, *J. Phys. Chem. A* 114 (2010) 3909–3915.
- [42] O. Thion, K. Rachedi, F. Diehl, P. Avenier, Y. Schuurman, Kinetics and mechanism of the water-gas shift reaction over platinum supported catalysts, *Top. Catal.* 52 (2009) 1940–1945, <http://dx.doi.org/10.1007/s11244-009-9377-z>.
- [43] M.A. Henderson, C.L. Perkins, M.H. Engelhard, S. Thevuthasan, C.H.F. Peden, Redox properties of water on the oxidized and reduced surfaces of CeO₂(1 1), *Surf. Sci.* 526 (2003) 1–18, [http://dx.doi.org/10.1016/S0039-6028\(02\)02657-2](http://dx.doi.org/10.1016/S0039-6028(02)02657-2).